1 **Cyclic CO_2 – H_2O injection and residual trapping: implications for CO_2 injection**

2 **efficiency and storage security**

3

4 Edlmann K.[1], Hinchliffe S.[1], Heinemann N.[1], Johnson G.[1], Ennis-King J.[2] and McDermott

5 C.I.[1]

6

7 *[1]School of GeoSciences, University of Edinburgh, Grant Institute, The King's Buildings,*

8 *University of Edinburgh, James Hutton Road, Edinburgh, EH9 3FE. United Kingdom.*

9 *[2]CSIRO Energy, Private Bag 10, Clayton South VIC 3169, Australia.*

10

11 **Corresponding Author**

12 Katriona Edlmann: School of Geoscience, Grant Institute, The King's Buildings, University of

13 Edinburgh, James Hutton Road, Edinburgh, EH9 3FE, United Kingdom.

14 kedlmann@staffmail.ed.ac.uk

15 Telephone: +44 (0) 131-650-7339

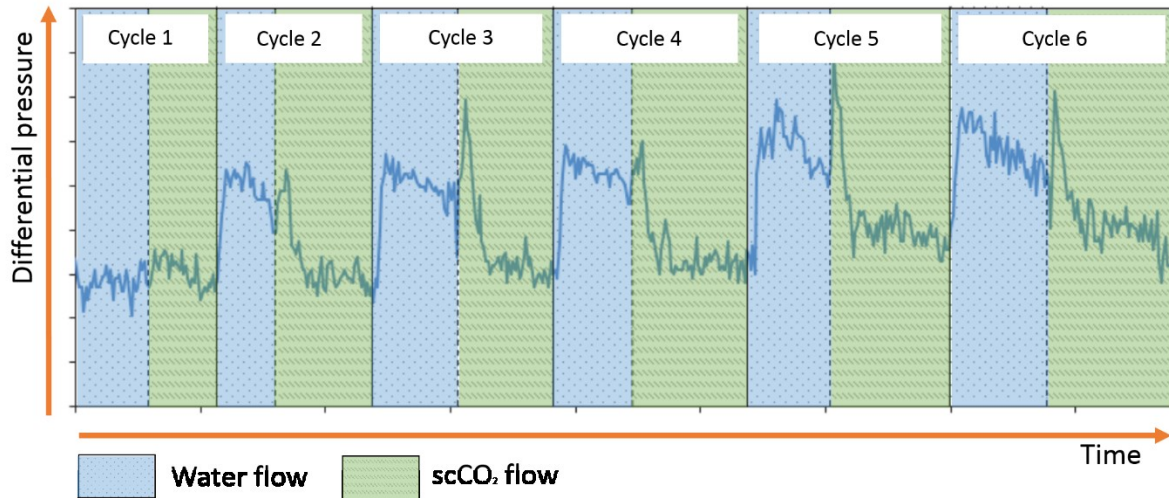16 Fax: +44 (0) 131-668-3184

17

18

19

20

21

22

23

Graphical abstract

25

Abstract

27   To meet the Paris Agreement target of limiting global warming to 2°C or below it is widely

28   accepted that Carbon Capture and Storage (CCS) will have to be deployed at scale. For the

29   first time, experiments have been undertaken over six cycles of water and supercritical CO_2

30   injection using a state of the art high flow rig recreating in-situ conditions of near wellbore

31   injection into analogue storage reservoir rocks. The results show that differential pressure

32   continuously increases over multiple injection cycles. Our interpretation is that multiple

33   cycles of injection result in a reduced effective permeability due to increased residual

34   trapping acting as a barrier to flow resulting in reduced injectivity. This is supported by

35   numerical modelling and field observations that show CO_2 injectivity and its variation over

36   time will be affected by multiple cycles of injection. These results suggest that loss of

37   injectivity must be incorporated into the injection strategy and that careful management of

38   cyclic injection will create the opportunity to increase residual trapping.

39   **1. Introduction**

40   The injection and storage of CO_2 into deep saline aquifers could make a significant

41   contribution to reducing global greenhouse emissions (Bachu and Adams, 2003; Benson

42 and Cole, 2008; Edlmann et al., 2015; Heinemann et al., 2018; IEA, 2004; Koide et al., 1992;

43 Metz, Davidson, de Coninck, 2005). Current field experience (Alcalde et al., 2017; Hosa et

44 al., 2011) suggests that a single well can inject in excess of 1MT of CO_2 per year with

45 numerical simulations indicating that during constant CO_2 injection, these injectivity rates can

46 be maintained (Heath et al., 2014; Jikich et al., 2003; Rutqvist et al., 2008; Zoback and

47 Gorelick, 2012). However, due to multiple input sources of CO_2, alternating CO_2 / brine

48 injection strategies, periodic injection and varying injection rates along with well maintenance

49 and workovers, a constant maintained injection strategy over a ~30 year project lifetime is

50 unlikely. Field experience from CO_2-EOR projects using water alternating gas injection

51 (WAG) have shown that a 20% loss of injectivity over the well life can be expected (Potter et

52 al., 1992; Schneider and Owens, 1976; Sohrabi et al., 2005). This suggests that ensuring

53 CO_2 injectivity can be maintained will require careful understanding of the fluid pressure

54 response to cyclic injection over time (Burton et al., 2008). Fluid mobility has a direct impact

55 on the injectivity of a well because fluid mobility is reduced in a multiphase system leading to

56 higher fluid pressures (Bachu, 2008; Dullien, 1992; Edlmann et al., 2013; Heinemann et al.,

57 2012; Morris et al., 2011). This means that to maintain injection rates higher pressures will

58 be experienced, which is, however, limited by fracturing pressure, which if exceeded has the

59 potential to open flow paths through which the CO_2 could escape (Edlmann et al., 2016;

60 McDermott et al., 2013; Smart et al., 2001).

61 The limited cyclic CO_2 / water (or brine) injection experiments on the multiphase flow

62 characteristics of CO_2 injection in the literature generally do not extend beyond two cycles

63 (Edlmann et al., 2013; Gamadi et al., 2014; Grigg and Svec, 2006, 2007; Larsen A., 1995;

64 Ma et al., 2016). Saeedi et al. undertook four cycles of injection and found that there were

65 notable hysteresis effects on injectivity during cyclic CO_2 - brine injection (Saeedi et al.,

66 2011). They suggested that this hysteresis effect may be limited to the first and second

67 flooding cycles.

68 In this paper, we present the results of six cycles of CO_2 - brine injection. Our experiments

69 have been designed using water unsaturated with respect to CO_2 to concentrate our focus

70 on the near well bore injection area and in particular the response of the bottom hole /

71 injection pressure. We find that for both the CO_2 and water injection cycles, the differential

72 pressure increases with each injection cycle and that the hysteresis effect is progressive.

73 Fluid mobility, which controls the differential pressure in the experiments, is influenced by (1)

74 pore space geometry, (2) wettability characteristics, and (3) the residual saturation of each

75 fluid phase. We investigate all three of these influences to determine which is responsible for

76 the increase in differential pressure and confirm our interpretation by numerically simulating

77 the experiments and by reviewing real-world CO_2 injection operations. The following sections

78 present the equipment summary, the experimental methodology, fluid properties, sample

79 characterisation, and the numerical simulation techniques. These have been designed to

80 minimise the potential for the sample pore network and mineralogy to impart significant

81 capillary pressure, mineral reactivity, clay mobilisation, wettability or thermal alteration

82 influences that may be possible explanations for the changes in permeability. This enables

83 us to suggest that the most likely explanation for the observed changes in permeability is

84 changes in residual trapping during multiple cycles of CO_2 and water injection.

85 **2. Materials and methods**

86 The experimental rig was designed to recreate subsurface near wellbore CO_2 injection

87 conditions. The equipment consists of a Hassler-type pressure vessel which holds cylindrical

88 rock samples of 38mm diameter within a pressurised rubber sleeve that applies the confining

89 pressure. A pair of Teledyne ISCO syringe pumps at the upstream end of the fluid system

90 control the flow rate of CO_2 and a HPLC water pump controls the flow rate of water. A

91 second pair of syringe pumps on the downstream end of the fluid system work in constant

92 pressure mode to control the fluid pressure. The core holder is contained within an oven,

93 allowing the temperature of the sample to be controlled and maintained. Full details of the

94 experimental equipment and considerations are given in the Supporting Information (SI).

95 Saturation tracking and fluid collection was not possible within the experimental setup. To

96 recreate subsurface injection conditions as closely as possible, the experiment was run with

97 supercritical phase CO_2. To achieve this, the rock and fluid temperature was set to 40°C, the

98 pore / fluid pressure at 10MPa, the confining pressure at 20MPa and the flow rate for both

99 the water and CO_2 pumps set to 1ml/min.

2.1. Experimental methodology

101 After injecting water through the sample to steady state flow for at least 15 minutes (primary

102 imbibition phase), the water injection is stopped and CO_2 injection initiated (primary drainage

103 phase), maintaining steady state CO_2 injection for at least 15 minutes. The second cycle

104 then begins by stopping the CO_2 injection and re-initiating the water injection (secondary

105 imbibition phase), maintaining steady-state water injection for at least 15 minutes followed by

106 CO_2 injection (secondary drainage phase), again maintaining steady state CO_2 injection for

107 at least 15 minutes. This sequence was repeated for six cycles of alternating CO_2 and water

108 injection. The detailed experimental process cycle for the flow experiments and the exact

109 timings of the flow cycles are provided in the SI.

2.2. Fluid properties

111 The two fluids used during the cyclic experimental work were de-ionised water (unsaturated

112 with respect to CO_2) as a proxy for brine and supercritical CO_2. The mass flow rate of water

113 is in parity with the volumetric flow rate, assuming at 40°C and 10MPa the water density is

114 992.2kg/m^3 and dynamic viscosity is 6.53 x10^{-4}Pa.s (Suekane, 2008). The ISCO CO_2 syringe

115 pump pressure was maintained at 10MPa and at a temperature of 5°C to ensure pump

116 efficiency (CO_2 density of 947.3kg/m^3 at 10MPa and 5°C) therefore the mass flow rate

117 leaving the pump is close to 1ml/min. However, the temperature of the CO_2 fluid entering

118 the core sample passes through a heat exchanger at oven at 40°C where the CO_2 density is

119 628.7kg/m^3 at 10MPa with a dynamic viscosity of 4.82 x10^{-5}Pa.s. This results in a change in

120 the volumetric flow rate through the sample. The flow rate of CO_2 through the sample was

121 estimated using mass conservation from the pump mass flow rate (1ml/min) multiplied by the

122 density ratio of the syringe pump CO_2 over the sample inlet CO_2 (947.3 / 628.7 = 1.5),

123 resulting in a volumetric flow rate for CO_2 into the sample of 1.5ml/min.

124 The solubility of CO_2 is controlled by temperature, pressure, and concentration of dissolved

125 matter. Under the experimental conditions the CO_2 solubility is approximately 54.9kg per

126 1000kg of unsaturated water, so 1 pore volume of water can dissolve 0.087 pore volumes of

127 CO_2.

128 **2.3. Sample Characterisation**

129 The experiment was conducted on Fell sandstone, a homogeneous quartz rich sandstone

130 and suitable UK North Sea aquifer storage analogue (Heinemann et al., 2013; Lewicki et al.,

131 2007; McDermott et al., 2017). It was chosen as it has an open pore network and is primarily

132 composed of quartz, minimising the potential for significant capillary pressure or mineral

133 reactivity influences, thereby enabling us to concentrate on the multiphase fluid response.

134 The experiment was conducted on a 38mm diameter and 80mm long cylindrical sample of

135 Fell sandstone, with a helium porosity of 20.3%, implying a pore volume of 18.4ml. The

136 sample intrinsic permeability to water of 26.24mD was measured at the beginning of the

137 experiment. These porosity and permeability values correspond well to those encountered

138 within the most likely UK and US CO_2 storage reservoir formations: Rotliegends (13 to 18%

139 porosity and 76.8 to 322mD (Glennie, 1990)); Bunter sandstone (15 to 26% porosity and 100

140 to 700mD (Abbotts, 1991; Reynolds et al., 2018)); Deactur Mt Simon sandstone (13 to

141 22.4% porosity and 26.4mD to 1D permeability (Frailey et al., 2011)); Goldeneye Captain

142 sandstone (~26% porosity and 1.1 to 7D permeability (McDermott et al., 2016; Reynolds et

143 al., 2018)); Sleipner Utsira sandstone (27 to 42% porosity and 1-3D permeability (Chadwick

144 et al., 2004)) and the Ormskirk sandstone (27% porosity and 0.0001 to >1D permeability

145 (Meadows and Beach, 1993; Reynolds et al., 2018)).

146

147

2.3.1. Sample mineralogy

The mineralogical composition of the sandstone was determined using X-Ray Diffraction

(XRD) before and after the experiment, supplemented by optical microscopy and Scanning

Electron Microscope (SEM) investigations to assess whether there was chemical reactivity

that could impact on the pore space geometry. The Fell sandstone is primarily quartz (93%)

with microcline (2%), illite (1.2%), kaolinite (1%) and calcite (0.1%). Detailed SEM images

and the XRD mineral abundances before and after the experiment are given in the SI.

2.3.2. Pore space geometry analysis

There is a large body of work that relates pore size and shape to capillary pressure, relative

permeability and hysteresis, where capillary pressure decreases as pore throat radius

increases (Dullien, 1992; Garcia et al., 2009; Jerauld and Salter, 1990; Pittman, 1992). Pore

shape analysis of the Fell sandstone was calculated on four images over three

magnifications obtained from the optical microscope (OM) and backscattered (BS) SEM

images with the full results available in section 5 of the SI. The image analysis results show

that the majority of the pores are between 100µm to 400µm in size. Gamma (γ) values for

the Fell sandstone, which expresses the roundness of a pore, with 1 a perfect sphere and

the pore space becomes increasingly complex and diverging as γ increases (Anselmetti,

F.S., Luthi, 1998) are between 2 and 4 which indicates the pores are relatively simple and

well rounded. γ increases as pore size increases suggesting the smaller pores are well-

rounded becoming slightly more complex with increasing size. This implies that the

influence of pore geometry does not inhibit fluid mobility, hence its influence on fluid flow

characteristics will be minimal and will not significantly influence the effective permeability

results. Full details of the pore space geometry analysis are presented in the SI.

2.4. Numerical simulation

Cyclic injection of different fluid phases will cause a hysteresis effect. Capillary forces within each of the drainage and imbibition cycles cause some of the non-wetting CO_2 to become disconnected, through snap-off, immobilised and residually trapped.

The first part of the numerical modelling fits a hysteretic model directly to the experimental data, in order to judge whether the observed behaviour fits within a standard paradigm. The hysteretic model for relative permeability and capillary pressure is outlined by Doughty (Doughty, 2007) and implemented in the inverse modelling code iTOUGH2 (Finsterle, 2004). The core is modelled as homogeneous cylinder of rock, and it is assumed that variations in saturation only occur along the axial direction i.e. the problem is one dimensional. The rates and timing of injection of water and CO_2 are taken directly from the experiment, and the model is fitted to experimental pressures at chosen calibration points (six per cycle) by adjusting the parameters of the hysteresis model through inversion algorithms.

It has been observed in core floods that due to the time scales of CO_2/water equilibration within the pore space relative to the flow velocity, the water that flows out of the core may be less than fully saturated with CO_2. Thus the standard assumption in the simulator of local equilibrium between phases may not reflect the experimental situation, and reduced dissolution could potentially lead to increasing CO_2 saturation across cycles. In these experiments there is no direct measurement of the concentration of CO_2 in the outflow and it is uncertain if the water injected during the experiments was fully saturated with CO_2 as it is simulated using the numerical simulators. The effect of this non-equilibrium in CO_2 and water dissolution can be partially mimicked in the simulations in a simple way by reducing the effective solubility of CO_2 in water. As a reference case, one simulation with a CO_2 solubility reduced to 50% of the bulk value at the experimental P, T conditions was run.

The second part of the numerical modelling examines whether the observed increase in differential pressure could be due to an enhancement of the hysteresis beyond the model

199   just discussed. An alternative model for CO_2 saturation has been devised in which the

200   residual gas saturation for imbibition is increased for each cycle. The reservoir engineering

201   software Eclipse 300 (Schlumberger) (Heinemann et al., 2016; Pickup et al., 2012), was

202   used in this study with the CO_2STORE option based on a modified Peng-Robinson equation

203   of state (Peng and Robinson, 1976) that allows for the mutual solubility of CO_2 and water.

204   Because it is the purpose of the simulations to show that the differential pressure increase

205   during cyclic CO_2 and water injection can be due to an increase in residual gas saturation,

206   mathematical relative permeability curves adopted from (van Genuchten, 1980) and (Corey,

207   1954) were used:

208 $$k_{rl} = \sqrt{S^*}\{1 - (1 - [S^*]^{1/m})^m\}^2 \qquad [1]$$

209    $$k_{rg} = (1 - S')^2(1 - S'^2) \qquad [2]$$

210   Where

211    $$S^* = (S_1 - S_{lr})/(1 - S_{lr}) \qquad [3]$$

212    $$S' = (S_1 - S_{lr})/(1 - S_{lr} - S_{gr}) \qquad [4]$$

213   The irreducible water saturation (S_{lr}) is initially set to 0.1, the residual gas saturation (S_{gr}) set

214   to 0.05 and the parameter m set to 0.6269 according to (Xu et al., 2003) for sand. To model

215   the hysteresis effect during the first injection cycle, the residual gas saturation for imbibition

216   (S_{gri}) was set to 0.2 and is then increased by 0.1 for each cycle (Figure 1). This systematic

217   increase is not based on experimental data or fitted to the increase in differential pressure

218   observed during the experiments described in this study. However, it shows that a stepwise

219   increase in residual gas saturation leads to an increase of the differential pressure. Capillary

220   pressure has been neglected.

221
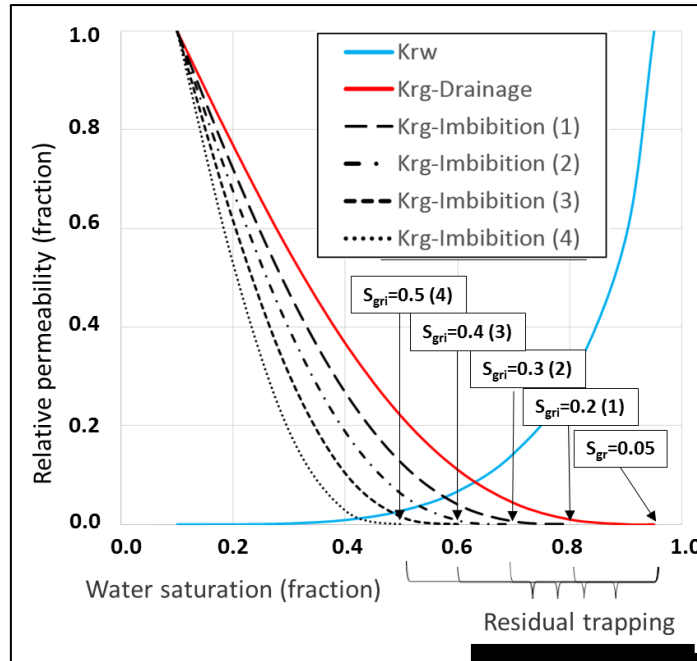
Figure 1 The relative permeability curves for water (krw – blue) and CO_2 (krg – red). The

residual saturation for the imbibition process (Sgri) for the four modelled injection cycles

*increases with every cycle (the cycle number in brackets).*

3. Results

3.1. Differential pressure evolution during cyclic CO_2 and water injection

Figure 2 presents the differential pressure response over all six $scCO_2$ / water flow cycle

experiments. There is a progressive increase in differential pressure (reduction in fluid

mobility) over the six cycles for both fluid phases. For the water phase, the average

differential pressure nearly doubled from 5.6psi in cycle 1 to 11.3psi in cycle 6. For the

$scCO_2$ phase, the average differential pressure increased from 6.3psi in cycle 1 to 8.1psi in

cycle 6. Interestingly the water, which is considered to be the wetting phase, has a higher

differential pressure than the $scCO_2$ and this is explored in more detail in Section 4.

Looking at the results of the water injection cycles (imbibition) in Figure 2 we see that after a

$scCO_2$ injection cycle as water is injected there is a sharp increase in differential pressure

(decrease in fluid mobility), followed by a slow reduction in differential pressure until the next

cycle. For the $scCO_2$ injection cycles (drainage) we see that after a water injection cycle, as

scCO₂ is injected, there is a significant increase in differential pressure followed immediately by a sharp fall in differential pressure (an increase in fluid mobility) to a differential pressure below that of the previous water cycle. There is then no significant change in differential pressure over each scCO₂ injection period, suggesting that once the scCO₂ is connected it maintains a stable flow path.
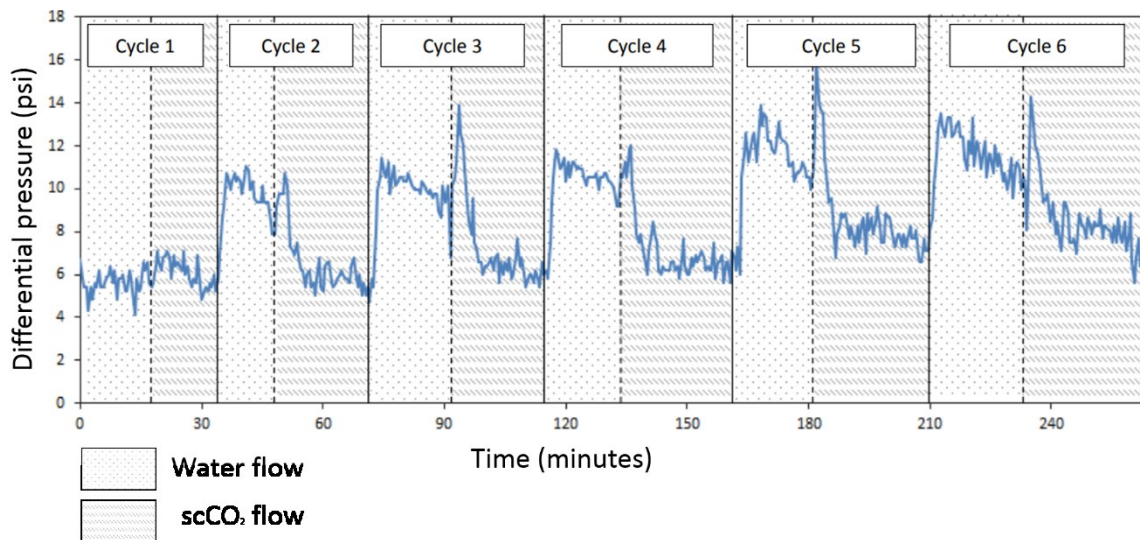
Figure 2 Differential pressure results during cyclic flow for the Fell Sandstone sample. The cycle number is indicated at the top of the graph. The relevant fluid flow within each cycle is indicated in the key. The differential pressure response is plotted as a 5 point moving average (which equates to a 30 second average) and more detail of this and the associated errors are given in the SI.

3.2. Mineralogy and pore geometry analysis

Full XRD and optical microscopy results for the Fell sandstone for both the pre and post brine - CO₂ flooding experiments are presented in the SI. There is only a small amount of reactive carbonates such as calcite (0.1%) which limits the potential for carbonate dissolution processes within the rock. There are no swelling or reactive clays present (such as montmorillonite) which could have an impact on the flow path of CO₂ by obstructing pore throats through the remobilisation of fine clay particles within the limited timeframe of the experiments (Dávila et al., 2017; Kampman et al., 2014). There are minor amounts of

257 kaolinite (1wt%) and Illite 1.3wt% which some researchers have shown will deflocculate or

258 exhibit minor swelling in water or brine (Aksu et al., 2015; Baptist and Sweeney, 1947; Dodd

259 et al., 1954; Leone and Scott, 1988). The sample preparation methodology of vacuum

260 saturating the sample for a week prior to the experiments have been designed to minimise

261 the impact of this potential swelling during the short duration experiments. The reduction in

262 pH associated with CO_2 dissolution into the water during the experiment will further reduce

263 the impact of any clay swelling, particularly in the kaolinite as the dispersion of clays is

264 minimised at low pH (Mohan and Fogler, 1997; Mungan, 1965; Simon et al., 1976; Valdya

265 and Fogler, 1992; van Oplhen H, 1964).

266 The post-experiment results show minor changes to some minerals after the flow

267 experiments, but in all cases, the percentage mineral change is smaller than the presented

268 standard deviation of the samples. Pre and post-experiment optical microscope

269 photographs of the injection surface of the rock sample also show no mineralogical or

270 thermal alteration within the samples. We conclude that there is minimal mineral reactivity or

271 thermal alteration during the experiment that could alter the pore space, pore throat

272 geometry and as such fluid response. This reinforces our interpretation that the pore

273 geometry does not inhibit or restrict the fluid mobility, and as such, the differential pressure

274 during cyclic CO_2 and water injection.

275 **4. Discussion of results**

276 Wettability is the tendency of one fluid to "wet" or adhere to the surface of a solid in the

277 presence of another immiscible fluid, termed the wetting and non-wetting fluid phase

278 respectively. Wettability can be quantified by determining the contact angle between the

279 wetting fluid and the solid surface involved (Aarnes et al., 2009; Dullien, 1992) and therefore

280 is a function of the rock mineralogy as well as the fluid. The capillary threshold pressure is

281 the pressure that must be overcome before a non-wetting phase will penetrate and flow

282 within the connected pore network and is dependent on the interfacial tension between the

283 wetting and non-wetting fluids, the contact angle between the mineral and fluid phase and

284 the pore throat radius. When a non-wetting phase is injected into a system the differential

285 pressure will increase until the capillary threshold pressure is exceeded. Once the capillary

286 threshold pressure has been exceeded, a continuous migration pathway can be created

287 through which the non-wetting phase can flow and the pressure will drop to an almost

288 constant value. Therefore, the pressure response in the experiments presented here can be

289 used to infer the wettability of the system and whether a change in wettability may be the

290 cause of the increasing pressure observed over the 6 cycles.

291 Firstly, the magnitude of the differential pressure measured when injecting the two phases

292 (CO_2 and water) could be used to infer the wettability with the lower differential pressure

293 corresponding with the wetting phase. However, this may not be conclusively diagnostic due

294 to other effects discussed below. Secondly, the rate of change of the differential pressure

295 during the cycle can be used to determine the wetting phase of the experiment. Here, the

296 rate of change of the differential pressure within each cycle can provide an indication of the

297 multiphase flow properties of both the water and $scCO_2$ during each cycle. If the rock and

298 fluid properties are constant, the changes in differential pressures during injection is

299 controlled by capillary pressure and relative permeability. The permeability of one phase at

300 any given location will depend on the saturation of the other phase present along with

301 interactions with the pore network (Aarnes et al., 2009). If water is the wetting phase then in

302 each water flow section, the rate of change of the differential pressure over that period

303 should be faster than for the non-wetting fluid, e.g. CO_2. Lastly, if the wettability changes

304 over time the rate of change in the pressure response in each individual cycle would also

305 change. It has been shown in recent studies that the wettability of quartz surfaces can alter

306 from a strongly water-wet system towards a less water-wet system in the presence of $scCO_2$

307 (Chiquet et al., 2007; Saraji et al., 2013). As the Fell sandstone is 93% quartz, the possibility

308 of a change in wettability as the cause of the change in differential pressure during cyclic

309 injection must thus be taken into account.

310   In these experiments we predict the water to be the wetting phase. A possible explanation

311   for why the wetting fluid (water) has a higher differential pressure than the non-wetting

312    $scCO_2$ within each cycle could be related to the viscosity difference between the two fluids.

313   The $scCO_2$ is the more mobile phase as it has a lower viscosity (Bachu and Bennion, 2008).

314   This could lead to highly non-uniform displacement of the water leading to channelling of

315    $scCO_2$ through a few preferential flow paths (Saeedi et al., 2011) which could reduce the

316   differential pressure of the $scCO_2$ flow through the samples.

317   Figure 3 shows the rate of change in pressure in each phase for each cycle. To minimise the

318   effect of any experimental errors during the pump changeovers, the first and last minutes of

319   each cycle were discounted from the rate of change calculations. The median time for each

320   section was found and the ΔP was calculated for the selected time period either side of the

321   median time and a trendline added with its gradient used to observe changes to the ΔP over

322   time.
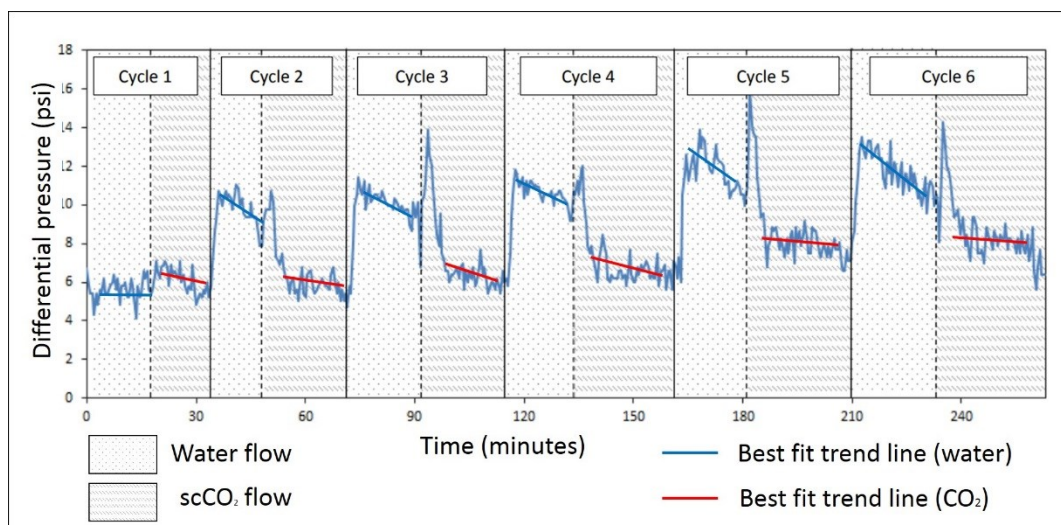
323

324   *Figure 3 The rate of change in the differential pressure for each fluid flow over all six cycles.*

325   Figure 2 shows that the reduction of the differential pressure during water injection is

326   relatively steep whereas the pressure during CO_2 injection increases dramatically and then

327   falls to a lower, barely changing level. This indicates that water is the wetting phase and CO_2

328   is the non-wetting phase throughout the experiments. It is therefore concluded from the rate

329   of change in pressure that the system is indeed water wet and that a wettability change from

330   water-wet to CO_2-wet is not responsible for the continuous increase in differential pressure

331   during cyclic water and CO_2 injection.

332   **4.1. Residual trapping**

333   Within a two-phase system the fraction of the pore space occupied by the wetting and non-

334   wetting phase is called the saturation, denoted S_w and S_{CO2} respectively:

335    $$S_w + S_{CO2} = 1 \qquad [5]$$

336   Where the non-wetting CO_2 phase can never reach either 0 or 1, due to the wetting water

337   phase adhering to the mineral surfaces. Hence, the two-phase system will actually range

338   from the critical water saturation S_{wc} to the maximum water saturation S_w^{max}.

339   If we consider the typical relative permeability function of water with respect to CO_2

340   saturation shown in Figure 1, it shows that the less CO_2 present, the higher the wetting

341   phase brine relative permeability, and vice versa. The curve shape is also dependant on flow

342   direction, whether it is undergoing drainage or imbibition. The curves are different as the

343   wetting and non-wetting phase take different flow paths through the network of pores.

344   During drainage the wetting fluid will preferentially fill the smaller pores and pore throats and

345   as the non-wetting fluid begins to flow as a continuous phase through the bigger pores,

346   occupying smaller pores as the non-wetting phase saturation increases. During this drainage

347   cycle, the wetting fluid (water) becomes increasingly reduced and eventually will be present

348   only as a thin film of residual water surrounding the edge of pores, termed irreducible water

349   saturation (S_{ir}). During the imbibition cycle when the wetting phase re-enters the pore

350   network, some of the non-wetting phase becomes gradually disconnected by the wetting

351   phase through capillary snap off and leads to residual trapping as the disconnected non-

352   wetting CO_2 become effectively immobile (Hesse et al., 2009). Each cycle imparts its own

353   change in the fluid saturation profile termed hysteresis (Juanes et al., 2006) which refers to

354   the dependence on the relative permeability to the previous saturation of the sample (Spiteri

355 and Juanes, 2006). Intuitively, as more and more non-wetting CO_2 phase enters through the

356 pore volume, the harder it will be for the wetting water phase to push it all out, as more and

357 more non-wetting CO_2 volume becomes trapped in the smaller pores.

358 If the injection cycle number is used as a proxy for decreasing water saturation in the core as

359 a result of an increasing amount of residually trapped CO_2 within the pore network, we can

360 create a proxy water relative permeability curve, full details are presented in the SI. The

361 water relative permeability curve shows a gradual decrease in effective permeability with

362 decreasing water saturation (increasing cycle number) which is consistent with the flow

363 experiment results that indicate that with multiple water / CO_2 injection cycles, increased

364 residual trapping acts as a barrier to flow and plays an important part in controlling

365 multiphase fluid dynamics during cyclic water / CO_2 injection.

366 This is important as it indicates that over the lifetime of a storage site, experiencing natural

367 cycles of fluid imbibition and drainage, the injectivity of the CO_2 may reduce over time,

368 leading to lower injection rates and/ or increased reservoir pressures.

369 **4.2. Residual saturation simulation analysis**

370 For the first stage of simulation, Figure 4 shows the fitting of a hysteresis model with

371 iTOUGH, where selected pressure points (shown as open circles) are used for the fit. The

372 details of the fitting parameters and the hysteresis model are discussed in the SI. If the

373 average data from just the first 4 cycles is used for the inverse model (solid green curve),

374 then the fit is moderate for those cycles, mainly because the differential pressure in these

375 cycles hardly changes in the experiments. However, when modelling the 5th and 6th cycle,

376 where the experiments show a significant increase in differential pressure, the model doesn't

377 capture the pressures increases, particularly during the CO_2 injection stages. Fitting to the

378 average of all 6 cycles doesn't markedly improve the overall quality of fit, and the model is

379 again unable to reproduce the increase in differential pressure over cycles – in each new

380 cycle after the second one, the model gives a very similar result to the previous cycle. This

381   indicates that the hysteresis model is unable to capture some features of the behaviour for

382   multiple injection cycles.

383   As discussed earlier, the effect of reduced effective solubility is also investigated, since

384   during water imbibition there is dissolution of CO_2 as well as displacement. Injection of water

385   for 30 minutes corresponds to 1.63 pore volumes, which could dissolve 0.14 pore volumes of

386   CO_2 assuming full saturation. The fitted results with the effective solubility at 50% of the bulk

387   value is shown as the dashed black curve. The pressure falloff during the water imbibition

388   stages is flatter in this model (since less CO_2 is dissolved over the injection cycle), but this

389   fails to improve the agreement with the experimental data, and indeed the fitted behaviour of

390   the 3rd-6th cycles closely follows the 2nd cycle. Thus reduced effective solubility is unable to

391   account for the observations.
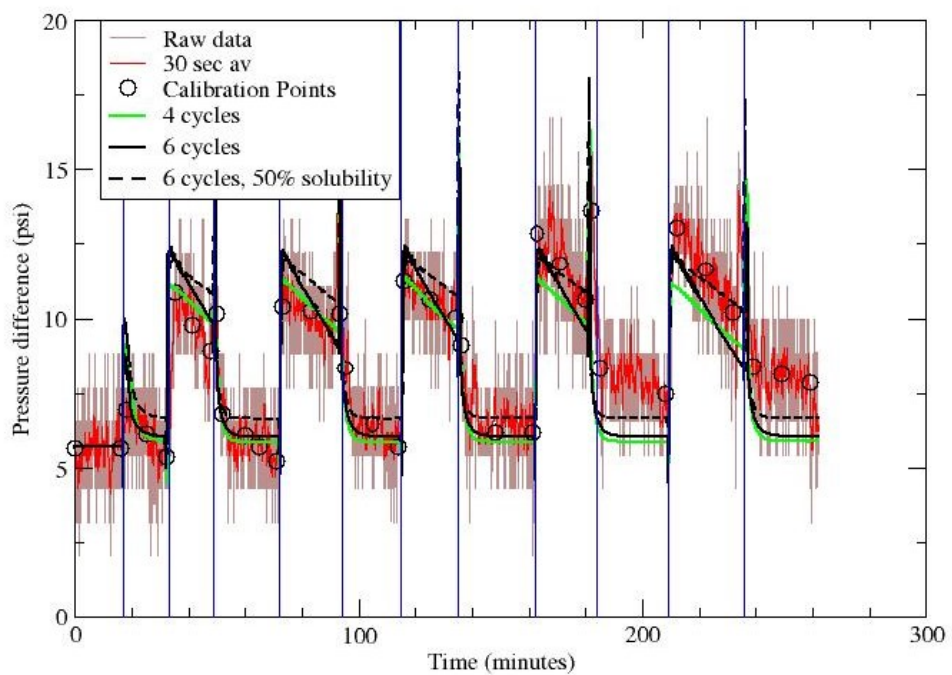
392

393   *Figure 4 Fitting of the experimental results to a hysteresis model with iTOUGH2. Brown*

394   *curve: The raw experimental data. Red curves: 30 second average of experimental data.*

395   *Open circles: calibration points for fit. Solid green curve: hysteresis model fitted to just the*

396   *first four cycles of water/CO_2 injection. Solid black curve: hysteresis model fitted to all six*

397 *cycles of water/CO_2 injection. Dashed black curve: hysteresis model fitted to all six cycles of*

398 *water/CO_2 injection but with reduced effective solubility 50% of bulk value.*

399 Saturation profiles along of the core are shown in Figure 5 for various points in the

400 simulation. The CO_2 saturation is almost identical after each CO_2 injection cycle (only the

401 profiles for the 1st and 6th cycles for clarity). When water is injected, there is a displacement

402 of CO_2 down to a residual value, which depends on the initial saturation at each point, in

403 accordance with the hysteresis model. There is also a dissolution front which moves along

404 the core from the inlet, and which assumes instantaneous dissolution at the front as

405 unsaturated water contacts CO_2. It can be seen in this Figure that the difference between the

406 water injection cycles is mainly due to their duration, since water injection for a longer

407 duration (e.g. the sixth cycle) propagates the dissolution front further from the inlet.

408 Changing the effective solubility slows the propagation of the dissolution front (not shown

409 here), so that it does not penetrate as far from the inlet over the duration of the water

410 injection cycle.
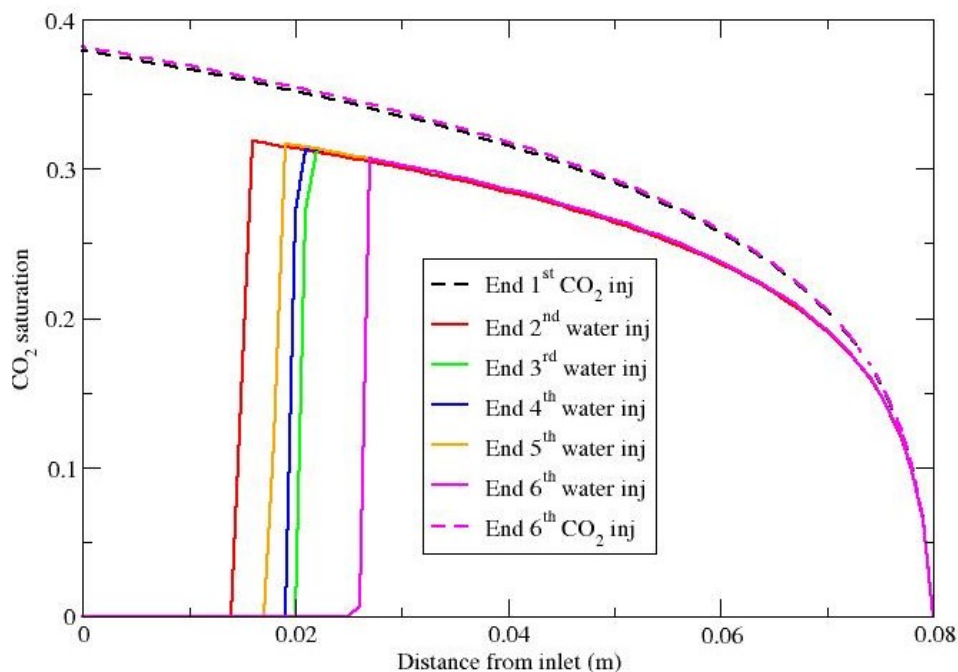
411

412 *Figure 5 CO_2 saturation profiles along the core during the TOUGH2 simulation, Dashed*
413 *black curve: end of 1st CO_2 injection. Solid red curve: end of 2nd water injection. Solid green*
414 *curve: end of 3rd water injection. Solid blue curve: End of 4th water injection. Solid orange*

415   *curve: end of 5th water injection. Solid magenta curve: end of 6th water injection. Dashed*
416   *magenta curve: end of 6th CO_2 injection.*

417   The evolution of CO_2 saturation in the simulation at various locations in the core is shown in

418   Figure 6. As seen in Figure 5 above, the saturation returns to the same level after each CO_2

419   injection. The next water injection then displaces CO_2 down to the residual saturation, which

420   depends on the initial saturation according to the hysteresis model. Locations within 0.02 m

421   of the inlet see the effect of the dissolution front during most of the water injection cycles,

422   when the gas saturation falls to zero. This region of zero saturation near the inlet

423   experiences no hysteresis on subsequent CO_2 injection. The fact that the CO_2 saturation

424   profiles in Figure 5 are nearly the same after each CO_2 injection explains why the pressure

425   response in the simulation to water injection is nearly the same in each cycle. This indicates

426   that the hysteresis effects in the model are not sufficient to represent all the experimental

427   observations
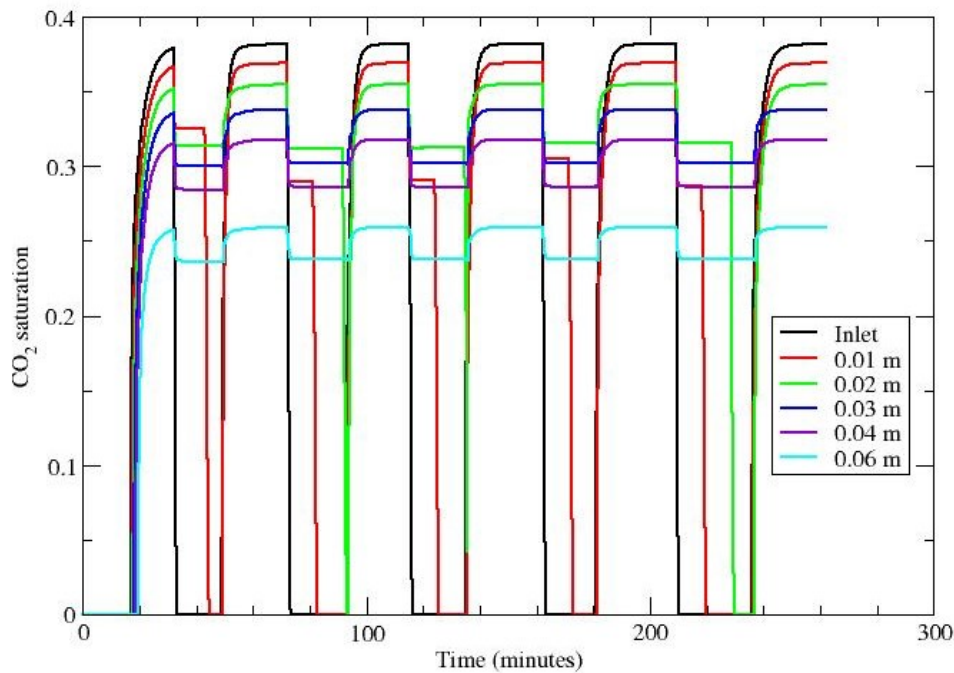
428

429   *Figure 6 Evolution of CO2 saturation with time in the TOUGH2 simulation at fixed locations*
430   *along the core, for the case fitted to the first 4 cycles of injection. Black line: Inlet. Red: 0.01*
431   *m from inlet. Green: 0.02 m. Blue: 0.03 m. Violet: 0.04m. Cyan: 0.06m.*

432

433   The result of the second stage of modelling, in which the residual trapping in the model is

434   deliberately increased between cycles (Figure 1), is shown in Figure 7. The comparison here

435   is qualitative, in that the simulation model parameters have not been fitted to the data. Two

436   similarities can be observed between the experimental results (Figure 2) and in the

437   modelling results (Figure 7). Firstly, the absolute increase in differential pressure during the

438   water injection period of cycles two, three and four, due to the increasing pore space

439   occupied by residually trapped CO_2 which then has to be pushed out by the invading water.

440   A greater or smaller increase in the residual saturation as the chosen 0.1 would lead to a

441   greater or smaller increase in differential pressure, respectively. Secondly, the increasing

442   rate of pressure decrease during the water injection period observed in the simulation results

443   can also be seen in the experimental results.
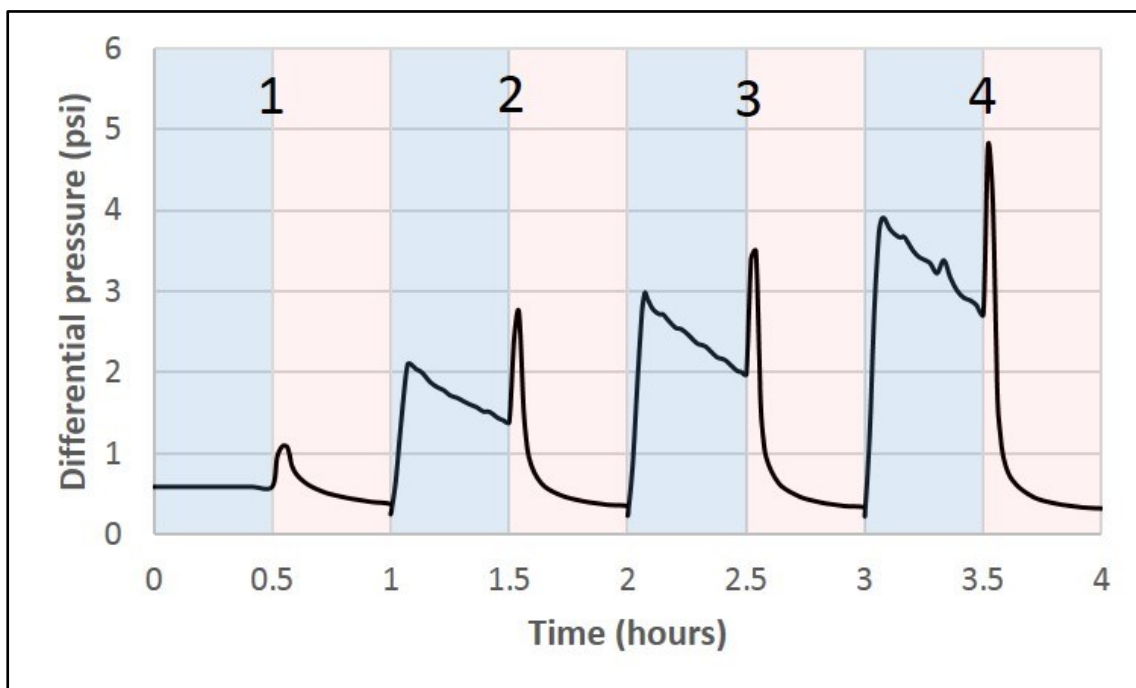
444

445   *Figure 7 The differential pressure throughout the injection cycles. Periods of water injection*

446   *are shaded in blue; periods of CO_2 injection are shaded in red. The cycle numbers are*

447   *highlighted in black, the imbibition residual gas saturation increases with every cycle (see*

448   *text for more information). Note the increase in differential pressure with increasing cycles.*

449   The simulation results show that an increase in residual CO_2 trapping could lead to an

450   increase in differential pressure during the water injection period. Hence the simulation

451   results are evidence for the hypothesis that a continuous increase of residually trapped CO_2

452   is responsible for the increase in differential pressure, and indicate that alternative hysteresis

453   models may be needed to incorporate this behaviour in numerical simulations.

454   **4.3. Field observations**

455   Field observations of cyclic water and CO_2 injection are primarily in enhanced oil recovery

456   (EOR) projects where the third fluid phase (hydrocarbon) and production of fluids

457   complicates the interpretation of the pressure profiles as pertaining to residual CO_2 (Eshiet

458   and Sheng, 2014; Gamadi et al., 2014; Hovorka, 2013; Kampman et al., 2014; Meyer, 2005;

459   Müller, 2011). However, a number of field experiments have been performed in CO_2 – brine

460   only systems that allow comparison with the experimental and modelling data presented

461   here. One of these is the CO2CRC Otway experiment in Victoria, Australia. Here, an

462   engineered residual trapping experiment was conducted twice, once in 2011 and once in

463   2014 (Ennis-King et al., 2017). The field experiment design is discussed in detail by Zhang

464   et al. (Zhang et al., 2011) but in summary, consists of creating a residually trapped CO_2 zone

465   within the formation by following CO_2 injection with CO_2 saturated water injection. Here

466   pressure response was monitored throughout all stages of injection including during baseline

467   characterisation tests (pre CO_2 injection) (Ennis-King et al., 2017). Hence the comparison of

468   pressure profiles during water injection into a water-saturated only and residually trapped

469   CO_2 formation is possible. Figure 8 compares the pressure response to water injection

470   before residual CO_2 is present (1st injection) and after it is present (2nd injection) for both the

471   2011 and 2014 tests. Note that the since the injection rates were not the same each time,

472   the pressures have been scaled to allow a proper comparison. The presence of the residual

473   CO_2 phase significantly increases the pressure build-up which is attributed to the lower

474   relative permeability to water at residual CO_2 saturation. This observation concurs with the

475   results from the modelling and experimental work presented above. The difference between

476 the reservoir response in the 2011 and 2014 tests may be due to alteration of the near-well

477 permeability, possible from sand production (Ennis-King et al., 2017a).
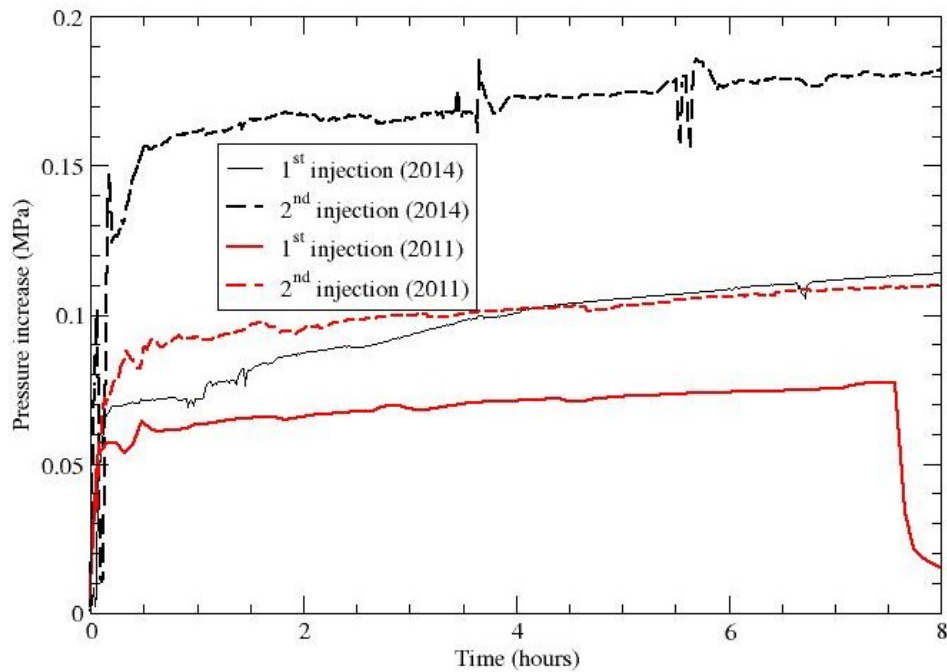
478

479 *Figure 8 Field data for pressure build-up during water injection before and after CO_2*

480 *injection. The single well test was carried out in 2011 and repeated in 2014. Since the*

481 *injection rates differ for each injection, the pressures have been scaled accordingly. Solid*

482 *black line: 1st injection (2014), 199 t/day (unscaled). Dashed black line: 2nd injection (2014),*

483 *rate 155 t/day, pressure scaled by 199/155. Solid red line: 1st injection (2011), 150 t/day,*

484 *pressure scaled by 199/150. Dashed red line: 2nd injection (2011), 191 t/day, pressure*

485 *scaled by 199/191.*

486 Modelling of enhanced trapping injection strategies including cyclic CO_2-water at the CO_2

487 field experiment in Israel (Heletz) (Rasmusson et al., 2016) is presented and discussed in

488 the SI, however, field results are not yet published so cannot be further compared here.

489

490

491

5. Conclusions

Our results clearly show, for the first time that the periodic injection of CO_2 over time may result in an increase in residually trapped CO_2. Our experiments and simulations are a direct analogue to deliberate operational changes (i.e. forced water injection) but they are equally applicable to periodic interruptions to CO_2 injection for example due to maintenance although this non forced imbibition (i.e. spontaneous water ingress with reduced injection pressure) may have a smaller effect than our experiments and simulations show. The results have implications that may benefit or hinder long-term CO_2 storage. On the one hand, increased residual trapping within the same pore space shows increased efficiency of storage operations and hence cost reductions (for example in monitoring a smaller areal footprint of CO_2 as compared to a plume of the same volume of CO_2 with lower saturations). Increased residual trapping also increases the storage security of an operation due to the reduced buoyant free-phase CO_2 that will be present. On the other hand, more residually trapped CO_2 in the vicinity of the well leads to more tortuous flow pathways for the injected CO_2 and hence to a pressure increase that may limit injectivity to within safe bounds. Hence a trade-off occurs between increased pore space utility and security of storage with injectivity and pressure increase. Our results thus will be of import to those deploying large scale and long-term storage and to those who regulate such operations.

6. Acknowledgements

518 **7. Supporting information**

519 The supporting information contains further detailed information on the experimental

520 equipment, considerations, and processes. The sample mineralogy and pore space

521 geometry analysis. The experimental relative permeability, residual saturation hysteresis,

522 model and fitting parameters and details of other field examples with CO_2 cyclic flow.

523 **8. References**

524 Aarnes, J.E., Lie, K.-A., Kippe, V., Krogstad, S., 2009. Multiscale methods for subsurface

525   flow, Multiscale modeling and …. https://doi.org/https://doi.org/10.1007/978-3-540-

526   88857-4_1

527 Abbotts, I.L., 1991. United Kingdom oil and gas fields : 25-years commemorative volume.

528   Geological Society.

529 Aksu, I., Bazilevskaya, E., Karpyn, Z.T., 2015. Swelling of clay minerals in unconsolidated

530   porous media and its impact on permeability. GeoResJ 7, 1–13.

531   https://doi.org/10.1016/J.GRJ.2015.02.003

532 Alcalde, J., Flude, S., Wilkinson, M., Johnson, G., Edlmann, K., Bond, C., Scott, V., Gilfillan,

533   S., Ogaya, X., Haszeldine, R., 2017. Quantifying geological CO2 storage security to

534   deliver on climate mitigation. Nat. Commun. Curr. Rev.

535   https://doi.org/10.17605/OSF.IO/X59QG

536 Anselmetti, F.S., Luthi, S. and E.G.P., 1998. Quantitative Characterization of Carbonate

537   Pore Systems by Digital Image Analysis. Am. Assoc. Pet. Geol. Bull. 10, 1815–1836.

538   https://doi.org/10.1306/1D9BD155-172D-11D7-8645000102C1865D

539 Bachu, S., 2008. CO2 storage in geological media: Role, means, status and barriers to

540   deployment. Prog. Energy Combust. Sci. 34, 254–273.

541   https://doi.org/10.1016/j.pecs.2007.10.001

542 Bachu, S., Adams, J.J., 2003. Sequestration of CO2 in geological media in response to

climate change: Capacity of deep saline aquifers to sequester CO2 in solution. Energy

Convers. Manag. 44, 3151–3175. https://doi.org/10.1016/S0196-8904(03)00101-8

Bachu, S., Bennion, B., 2008. Effects of in-situ conditions on relative permeability

characteristics of CO2-brine systems. Environ. Geol. 54, 1707–1722.

https://doi.org/10.1007/s00254-007-0946-9

Baptist, O.C., Sweeney, S.A., 1947. The effect of clays on the permeability of reservoir

sands to waters of different saline contents.

Benson, S.M., Cole, D.R., 2008. CO2 sequestration in deep sedimentary formations.

Elements 4, 325–331. https://doi.org/10.2113/gselements.4.5.325

Burton, M., Kumar, N., Bryant, S.L., 2008. Time-Dependent Injectivity During CO2 Storage in

Aquifers. SPE/DOE Fourteenth Symp. Improv. Oil Recover. Tulsa, Oklahoma, USA 19--

23 April 19–23. https://doi.org/10.2118/113937-MS

Chadwick, R.., Zweigel, P., Gregersen, U., Kirby, G.., Holloway, S., Johannessen, P.., 2004.

Geological reservoir characterization of a CO2 storage site: The Utsira Sand, Sleipner,

northern North Sea. Energy 29, 1371–1381.

https://doi.org/10.1016/J.ENERGY.2004.03.071

Chiquet, P., Broseta, D., Thibeau, S., 2007. Wettability alteration of caprock minerals by

carbon dioxide. Geofluids 7, 112–122. https://doi.org/10.1111/j.1468-

8123.2007.00168.x

Corey, A.T., 1954. The Interrelation Between Gas and Oil Relative Permeabilites, Producers

Monthly.

Dávila, G., Cama, J., Luquot, L., Soler, J.M., Ayora, C., 2017. Experimental and modeling

study of the interaction between a crushed marl caprock and CO2-rich solutions under

different pressure and temperature conditions. Chem. Geol. 448, 26–42.

https://doi.org/10.1016/j.chemgeo.2016.10.034

568   Dodd, C.G., Conley, F.R., Barnes, P.M., 1954. Clay minerals in petroleum reservoir sands

569   and water sensitivity effects. https://doi.org/10.1346/CCMN.1954.0030118

570   Doughty, C., 2007. Modeling geologic storage of carbon dioxide: Comparison of non-

571   hysteretic and hysteretic characteristic curves. Energy Convers. Manag. 48, 1768–

572   1781. https://doi.org/10.1016/J.ENCONMAN.2007.01.022

573   Dullien, F.A.L., 1992. Porous media : fluid transport and pore structure. Academic Press.

574   Edlmann, K., Bensabat, J., Niemi, A., Haszeldine, R.S., McDermott, C.I., 2016. Lessons

575   learned from using expert elicitation to identify, assess and rank the potential leakage

576   scenarios at the Heletz pilot CO_2 injection site. Int. J. Greenh. Gas Control 49, 473–

577   487. https://doi.org/10.1016/j.ijggc.2016.02.018

578   Edlmann, K., Edwards, M.A., Qiao, X.J., Haszeldine, R.S., McDermott, C.I., 2015. Appraisal

579   of global CO_2 storage opportunities using the geomechanical facies approach. Environ.

580   Earth Sci. 73, 8075–8096. https://doi.org/10.1007/s12665-014-3965-3

581   Edlmann, K., Haszeldine, S., McDermott, C.I.I., 2013. Experimental investigation into the

582   sealing capability of naturally fractured shale caprocks to supercritical carbon dioxide

583   flow. Environ. Earth Sci. 70, 3393–3409. https://doi.org/10.1007/s12665-013-2407-y

584   Ennis-King, J., LaForce, T., Paterson, L., Black, J.R., Vu, H.P., Haese, R.R., Serno, S.,

585   Gilfillan, S., Johnson, G., Freifeld, B., Singh, R., 2017a. Stepping into the Same River

586   Twice: Field Evidence for the Repeatability of a CO_2 Injection Test. Energy Procedia

587   114, 2760–2771. https://doi.org/10.1016/J.EGYPRO.2017.03.1392

588   Ennis-King, J., Laforce, T., Paterson, L., Dance, T., Jenkins, C., Cinar, Y., 2017b.

589   Interpretation of above zone and storage zone pressure responses to carbon dioxide

590   injection in the 2016 CO2CRC field test . Energy Procedia 114, 5671–5679.

591   https://doi.org/10.1016/j.egypro.2017.03.1706

592   Eshiet, K., Sheng, Y., 2014. Investigation of geomechanical responses of reservoirs induced

593   by carbon dioxide storage. Environ. Earth Sci. 71, 3999–4020.

594   https://doi.org/10.1007/s12665-013-2784-2

595   Finsterle, S., 2004. Multiphase Inverse Modeling. Vadose Zo. J. 3, 747.

596   https://doi.org/10.2136/vzj2004.0747

597   Frailey, S.M., Damico, J., Leetaru, H.E., 2011. Reservoir characterization of the Mt. Simon

598   Sandstone, Illinois Basin, USA. Energy Procedia 4, 5487–5494.

599   https://doi.org/10.1016/J.EGYPRO.2011.02.534

600   Gamadi, T.D., Sheng, J.J., Soliman, M.Y., Menouar, H., Watson, M.C., Emadibaladehi, H.,

601   2014. An Experimental Study of Cyclic CO_2 Injection to Improve Shale Oil Recovery, in:

602   SPE Improved Oil Recovery Symposium. Society of Petroleum Engineers.

603   https://doi.org/10.2118/169142-MS

604   Garcia, X., Akanji, L.T., Blunt, M.J., Matthai, S.K., Latham, J.P., 2009. Numerical study of the

605   effects of particle shape and polydispersity on permeability. Phys. Rev. E - Stat.

606   Nonlinear, Soft Matter Phys. 80, 1–9. https://doi.org/10.1103/PhysRevE.80.021304

607   Glennie, K.W., 1990. Introduction to the petroleum geology of the North Sea. Blackwell

608   Scientific Publications.

609   Grigg, R., Svec, R., 2006. CO_2 Transport Mechanisms in CO_2/Brine Coreflooding. Proc.

610   SPE Annu. Tech. Conf. Exhib. https://doi.org/10.2118/103228-MS

611   Grigg, R.B., Svec, R.K., 2007. CO_2 retention and injectivity changes : laboratory tests. Sixth

612   Annu. Conf. Carbon Capture Sequestration.

613   Heath, J.E., McKenna, S.A., Dewers, T.A., Roach, J.D., Kobos, P.H., 2014. Multiwell CO_2

614   injectivity: Impact of boundary conditions and brine extraction on geologic CO_2 storage

615   efficiency and pressure buildup. Environ. Sci. Technol. 48, 1067–1074.

616   https://doi.org/10.1021/es4017014

617   Heinemann, N., Booth, M.G., Haszeldine, R.S., Wilkinson, M., Scafidi, J. , Edlmann, K.,

618   2018. Hydrogen storage in porous geological formations – Onshore play opportunities

619   in the Midland Valley (Scotland, UK). https://doi.org/10.31223/osf.io/m4uw

620 Heinemann, N., Stewart, R.J., Wilkinson, M., Pickup, G.E.E., Haszeldine, R.S.S., 2016.

621   Hydrodynamics in subsurface CO2 storage: Tilted contacts and increased storage

622   security. Int. J. Greenh. Gas Control 54, 322–329.

623   https://doi.org/10.1016/j.ijggc.2016.10.003

624 Heinemann, N., Wilkinson, M., Haszeldine, R.S., Fallick, A.E., Pickup, G.E., 2013. CO2

625   sequestration in a UK North Sea analogue for geological carbon storage. Geology 41,

626   411–414. https://doi.org/10.1130/G33835.1

627 Heinemann, N., Wilkinson, M., Pickup, G.E., Haszeldine, R.S., Cutler, N.A., 2012. CO 2

628   storage in the offshore UK Bunter Sandstone Formation. Int. J. Greenh. Gas Control 6,

629   210–219. https://doi.org/10.1016/j.ijggc.2011.11.002

630 Hesse, M.A., Orr, F.M., Tchelepi, H.A., 2009. Gravity currents with residual trapping. Energy

631   Procedia 1, 3275–3281. https://doi.org/10.1016/j.egypro.2009.02.113

632 Hosa, A., Esentia, M., Stewart, J., Haszeldine, S., 2011. Injection of CO2 into saline

633   formations: Benchmarking worldwide projects.

634   https://doi.org/10.1016/j.cherd.2011.04.003

635 Hovorka, S.D., 2013. EOR as Sequestration — Geoscience Perspective.

636 IEA, 2004. Energy Technology Analysis: Prospects for CO2 Capture and Storage.

637   https://doi.org/10.1016/B978-1-85617-710-8.00010-8

638 Jerauld, G.R., Salter, S.J., 1990. The Effect of Pore Structure on Hysteresis in Relative

639   Permeability and Capillary Pressure: Pore Level Modeling. Transp. Porous Media 5,

640   103.

641 Jikich, S. a., Sams, W.N., Bromhal, G., Pope, G., Gupta, N., Smith, D.H., 2003. Carbon

642   dioxide injectivity in brine reservoirs using horizontal wells. Second Annu. Conf. carbon

643 sequestration, Dev. validating Technol. base to reduce carbon intensity, Alexandria,

644 Virginia 5–8.

645 Juanes, R., Spiteri, E.J., Orr, F.M., Blunt, M.J., 2006. Impact of relative permeability

646 hysteresis on geological CO2 storage. Water Resour. Res. 42, 1–13.

647 https://doi.org/10.1029/2005WR004806

648 Kampman, N., Bickle, M., Wigley, M., Dubacq, B., 2014. Fluid flow and CO2-fluid-mineral

649 interactions during CO2-storage in sedimentary basins. Chem. Geol. 369, 22–50.

650 https://doi.org/10.1016/j.chemgeo.2013.11.012

651 Koide, H., Tazaki, Y., Noguchi, Y., Nakayama, S., Iijima, M., Ito, K., Shindo, Y., 1992.

652 Subterranean containment and long-term storage of carbon dioxide in unused aquifers

653 and in depleted natural gas reservoirs. Energy Convers. Manag. 33, 619–626.

654 https://doi.org/10.1016/0196-8904(92)90064-4

655 Larsen A., J.A.. S., 1995. Comparing Hysteresis Models for Relative Permeability in WAG

656 Studies, Sca.

657 Leone, J.A., Scott, M.E., 1988. Characterization and Control of Formation Damage During

658 Waterflooding of a High-Clay-Content Reservoir. SPE Reserv. Eng. 3, 1279–1286.

659 https://doi.org/10.2118/16234-PA

660 Lewicki, J.L., Birkholzer, J., Tsang, C.F., 2007. Natural and industrial analogues for leakage

661 of CO2 from storage reservoirs: Identification of features, events, and processes and

662 lessons learned. Environ. Geol. 52, 457–467. https://doi.org/10.1007/s00254-006-0479-

663 7

664 Ma, J., Wang, X., Gao, R., Zeng, F., Huang, C., Tontiwachwuthikul, P., Liang, Z., 2016.

665 Study of cyclic CO2 injection for low-pressure light oil recovery under reservoir

666 conditions. Fuel 174, 296–306. https://doi.org/10.1016/J.FUEL.2016.02.017

667 McDermott, C., Williams, J., Tucker, O., Jin, M., Mackay, E., Edlmann, K., Haszeldine,

R.S.S., Wang, W., Kolditz, O., Akhurst, M., 2016. Screening the geomechanical stability (thermal and mechanical) of shared multi-user CO2 storage assets: A simple effective tool applied to the Captain Sandstone Aquifer. Int. J. Greenh. Gas Control 45, 43–61. https://doi.org/10.1016/j.ijggc.2015.11.025

McDermott, C.I., Miocic, J.M., Edlmann, K., Gilfillan, S.M.V., 2017. Natural analogue studies, in: Theory and Applications of Transport in Porous Media. https://doi.org/10.1007/978-94-024-0996-3_9

McDermott, C.I.I., Edlmann, K., Haszeldine, R.S.S., 2013. Predicting hydraulic tensile fracture spacing in strata-bound systems. Int. J. Rock Mech. Min. Sci. 63, 39–49. https://doi.org/10.1016/j.ijrmms.2013.06.004

Meadows, N.S., Beach, A., 1993. Controls on reservoir quality in the Triassic Sherwood Sandstone of the Irish Sea, in: Petroleum Geology of Northwest Europe: Proceedings of the 4th Conference. Geological Society of London, pp. 823–833. https://doi.org/10.1144/0040823

Metz, Davidson, de Coninck, L. and M., 2005. CARBON DIOXIDE CAPTURE AND STORAGE. Cambridge University press, New york.

Meyer, J.P., 2005. Summary of Carbon Dioxide Enhanced Oil Recovery (CO 2 EOR)Injection Well Technology Supporting. Am. Pet. Inst. 63. https://doi.org/http://www.api.org/~/media/Files/EHS/climate-change/Summary-carbon-dioxide-enhanced-oil-recovery-well-tech.pdf

Mohan, K.K., Fogler, H.S., 1997. Effect of pH and Layer Charge on Formation Damage in Porous Media Containing Swelling Clays.

Morris, J.P., Detwiler, R.L., Friedmann, S.J., Vorobiev, O.Y., Hao, Y., 2011. The large-scale geomechanical and hydrogeological effects of multiple CO2 injection sites on formation stability. Int. J. Greenh. Gas Control 5, 69–74.

693   https://doi.org/10.1016/j.ijggc.2010.07.006

694   Müller, N., 2011. Supercritical CO2-Brine Relative Permeability Experiments in Reservoir

695   Rocks-Literature Review and Recommendations. Transp. Porous Media 87, 367–383.

696   https://doi.org/10.1007/s11242-010-9689-2

697   Mungan, N., 1965. Permeability Reduction Through Changes in pH and Salinity. J. Pet.

698   Technol. 17, 1449–1453. https://doi.org/10.2118/1283-PA

699   Peng, D.Y., Robinson, D.B., 1976. A New Two-Constant Equation of State. Ind. Eng. Chem.

700   Fundam. 15, 59–64. https://doi.org/10.1021/i160057a011

701   Pickup, G.E., Mackay, E.J., Heinemann, N., Shariatipour, S.M., 2012. Flow simulation of CO

702   2 storage in saline aquifers using a black oil simulator. Carbon Manag. Technol. Conf.

703   [CMTC] (Orlando, FL, 2/7-9/2012) Proc. 1, 276–289. https://doi.org/10.7122/151042-

704   MS

705   Pittman, E.D., 1992. Relationship of porosity and permeability to various parameters derived

706   from mercury injection-capillary pressure curves for sandstone. Am. Assoc. Pet. Geol.

707   Bull. https://doi.org/10.1017/CBO9781107415324.004

708   Potter, G.F., Hadlow, R.E., Surguchev, L., Research, R., Korbel, R., Haugen, S., Krakstad,

709   O., Patel, P.D., Christman, P.G., Gardner, J.W., 1992. Update of Industry Experience

710   With CO2 Injection. SPE Annu. Tech. Conf. Exhib. 2, 507–513.

711   https://doi.org/10.2118/25075-MS

712   Rasmusson, K., Rasmusson, M., Tsang, Y., Niemi, A., 2016. A simulation study of the effect

713   of trapping model, geological heterogeneity and injection strategies on CO2 trapping.

714   Int. J. Greenh. Gas Control 52, 52–72. https://doi.org/10.1016/J.IJGGC.2016.06.020

715   Reynolds, C.A., Blunt, M.J., Krevor, S., 2018. Multiphase Flow Characteristics of

716   Heterogeneous Rocks From CO $_2$ Storage Reservoirs in the United Kingdom. Water

717   Resour. Res. 54, 729–745. https://doi.org/10.1002/2017WR021651

718   Rutqvist, J., Birkholzer, J.T., Tsang, C.F., 2008. Coupled reservoir-geomechanical analysis

719   of the potential for tensile and shear failure associated with CO2 injection in

720   multilayered reservoir-caprock systems. Int. J. Rock Mech. Min. Sci. 45, 132–143.

721   https://doi.org/10.1016/j.ijrmms.2007.04.006

722   Saeedi, A., Rezaee, R., Evans, B., Clennell, B., 2011. Multiphase flow behaviour during CO2

723   geo-sequestration: Emphasis on the effect of cyclic CO2-brine flooding. J. Pet. Sci.

724   Eng. 79, 65–85. https://doi.org/10.1016/j.petrol.2011.07.007

725   Saraji, S., Goual, L., Piri, M., Plancher, H., 2013. Wettability of supercritical carbon

726   dioxide/water/quartz systems: Simultaneous measurement of contact angle and

727   interfacial tension at reservoir conditions. Langmuir 29, 6856–6866.

728   https://doi.org/10.1021/la3050863

729   Schneider, F.N., Owens, W.W., 1976. Relative Permeability Studies of Gas-Water Flow

730   Following Solvent Injection in Carbonate Rocks. Soc. Pet. Eng. J. 16, 23–30.

731   https://doi.org/10.2118/5554-PA

732   Simon, D.E., McDaniel, B.W., Coon, R.M., 1976. Evaluation of Fluid pH Effects on Low

733   Permeability Sandstones, in: SPE Annual Fall Technical Conference and Exhibition.

734   Society of Petroleum Engineers. https://doi.org/10.2118/6010-MS

735   Smart, B.G.D., Somerville, J.M., Edlman, K., Jones, C., 2001. Stress sensitivity of fractured

736   reservoirs. J. Pet. Sci. Eng. 29, 29–37. https://doi.org/10.1016/S0920-4105(00)00088-7

737   Sohrabi, M., Danesh, A., Tehrani, D., 2005. Oil Recovery by Near-Miscible SWAG Injection.

738   Proc. SPE Eur. Annu. Conf. 24–26. https://doi.org/10.2523/94073-MS

739   Spiteri, E.J., Juanes, R., 2006. Impact of relative permeability hysteresis on the numerical

740   simulation of WAG injection. J. Pet. Sci. Eng. 50, 115–139.

741   https://doi.org/10.1016/j.petrol.2005.09.004

742   Suekane, 2008. Geological storage of carbon dioxide by residual gas and solubility trapping.

743 Int. J. Greenh. Gas Control 2, 58–64. https://doi.org/10.1016/S1750-5836(07)00096-5

744 Valdya, R.N., Fogler, H.S., 1992. Fines Migration and Formation Damage: Influence of pH

745 and Ion Exchange. SPE Prod. Eng. 7, 325–330. https://doi.org/10.2118/19413-PA

746 van Genuchten, M.T., 1980. A Closed-form Equation for Predicting the Hydraulic

747 Conductivity of Unsaturated Soils1. Soil Sci. Soc. Am. J. 44, 892.

748 https://doi.org/10.2136/sssaj1980.03615995004400050002x

749 van Oplhen H, 1964. An introduction to clay colloid chemistry. By H van Olphen. Interscience

750 Publishers, Div. of John Wiley & Sons, 605 Third Ave., New York 16, N. Y, 1963.

751 xvi + 301 pp. 15.5 × 23 cm. Price $10, Journal of Pharmaceutical Sciences. Elsevier.

752 https://doi.org/10.1002/JPS.2600530238

753 Xu, T., Apps, J.A., Pruess, K., 2003. Reactive geochemical transport simulation to study

754 mineral trapping for CO_2 disposal in deep arenaceous formations. J. Geophys. Res.

755 Solid Earth 108, 1–66. https://doi.org/10.1029/2002JB001979

756 Zhang, Y., Freifeld, B., Finsterle, S., Leahy, M., Ennis-King, J., Paterson, L., Dance, T.,

757 2011. Single-well experimental design for studying residual trapping of supercritical

758 carbon dioxide. Int. J. Greenh. Gas Control. Elsevier Ltd.

759 https://doi.org/10.1016/j.ijggc.2010.06.011

760 Zoback, M.D., Gorelick, S.M., 2012. Earthquake triggering and large-scale geologic storage

761 of carbon dioxide. Proc. Natl. Acad. Sci. 109, 10164–10168.

762 https://doi.org/10.1073/pnas.1202473109

763